DESIGN AND CONTROL OF A VARIABLE DISPLACEMENT VANE PUMP FOR VALVELESS HYDRAULIC ACTUATION

By

Tyler Bo Li

Dissertation
Submitted to the Faculty of the
Graduate School of Vanderbilt University in
partial fulfillment of the requirements
for the degree of
DOCTOR OF PHILOSOPHY
in
Mechanical Engineering
December, 2008
Nashville, Tennessee

Approved:

Professor Michael Goldfarb

Professor Eric Barth

Professor Nilanjan Sarkar

Professor George Cook

Professor Robert Webster

ACKNOWLEDGMENTS

The research work in this thesis was performed at the Center for Intelligent Mechatronics in the Department of Mechanical Engineering at Vanderbilt University. The author wishes to deeply thank his advisor, Dr. Michael Goldfarb, whose idea, vision, and constant support made this research possible. In addition, the author also would like to extend sincere appreciation to his committee member Dr. Eric Barth and to his colleagues Dr. Kevin Fite, Dr. Shengrong Shen, Abhijit Barman and Jason Mitchell, for their valuable inputs and contributions to this work.

Special thanks to my parents and to my wife Shanshan, who have been giving me everlasting love and support along the way and always being there for me. Nothing can be achieved without you in my life.

TABLE OF CONTENTS

Page

ACKNOWLEDGMENTS i

TABLE OF CONTENTS ii

LIST OF FIGURES iii

CHAPTER I INTRODUCTION 1

CHAPTER II DESIGN OF VARIABLE DISPLACEMENT VANE PUMP 6

Descriptions 6
Flow Rate Calculation and Sizing 13
Prototype Performance 18
Experimental Setup 21

CHAPTER III 23

PRELIMINARY CONTROL OF VDVP BASED HYDRAULIC ACTUATION SYSTEM 23

Linear Model of the VDVP Based Hydraulic Actuation System 23
PID and Smith Predictor Combined Controller Design 25
Experimental Results 25

CHAPTER IV ADVANCED CONTROL OF VDVP BASED HYDRAULIC ACTUATION SYSTEM 30

Nonlinear Model of the VDVP Based Hydraulic Actuation System 30
Identification of Model Parameters 32
Sliding Mode Control Design 36
Experimental Results 38

CHAPTER V EFFICIENCY OF VDVP BASED HYDRAULIC ACTUATION SYSTEM 43

CHAPTER VI CONCLUSION AND DISCUSSION 47

REFERENCE 48

LIST OF FIGURES

Table .....Page

Fig. 1-1. Schematic of a basic hydraulic actuation circuit. 2

Fig. 1-2. Schematic of a VDP-controlled hydraulic actuator. 3

Fig. 2-1. Basic mechanism of a variable displacement vane pump. 7

Fig. 2-2. The assembled view of the VDVP. 8

Fig. 2-3. The exploded view with all the mechanical parts of VDVP. 9

Fig. 2-4. The VDVP with the front half of pump body removed. 9

Fig. 2-5. A section view of the VDVP. 10

Fig. 2-6. The exploded view that shows the seals of VDVP. 10

Fig. 2-7. Slots for push rods in VDVP. 11

Fig. 2-8. Graphite rear end plate. 12

Fig. 2-9. Bearing assembly for lead screw. 12

Fig. 2-10. Stack of six variable displacement vane pumps for actuation of a six-axis machine. 13

Fig. 2-11. Schematic of cross-section when $x \geq 0$. 14

Fig. 2-12. Schematic of cross-section when $x \prec 0$ 14

Fig. 2-13. Schematic of cross-sectional area of vane. 16

Fig. 2-14. VDVP prototype (with a DC motor assembled). 18

Fig. 2-15. Step response of VDVP stator corresponding to ±50% of the stator motion. . 19

Fig. 2-16. Bandwidth of VDVP stator motion. 20

Fig. 2-17. Pump flow rate as a function of stator displacement at a shaft speed of 1750 RPM. 20

Fig. 2-18. Experimentally determined pump characteristics. 21

Fig. 2-19. Hydraulic circuit consists of VDVP and hydraulic cylinder. 22

Fig. 3-1. Experimentally determine the system transfer function. 24

Fig. 3-2. Smith Predictor. 25

Fig. 3-3. SP and PID: Step tracking. 26

Fig. 3-4. SP and PID: Sinusoidal signal tracking, 0.25 Hz 26

Fig. 3-5. SP and PID: Sinusoidal signal tracking, 0.5 Hz 27

Fig. 3-6. SP and PID: Sinusoidal signal tracking, 1 Hz. 27

Fig. 3-7. SP and PID: Sinusoidal signal tracking, 2 Hz. 28

Fig. 3-8. Compare tracking performance between using PID controller only and using SP&PID controller. 29

Fig. 4-1. Schematic of a hydraulic cylinder. 30

Fig. 4-2. Prediction error method. 33

Fig. 4-3. Experimental results in system identification. 34

Fig. 4-4. Parameter estimation with experimental results. 35

Fig. 4-5. Model validation based on the estimated parameters and experimental results. 35

Fig. 4-6. Step tracking of the sliding mode controller. 38

Fig. 4-7. Tracking performance of the sliding mode controller corresponding to a 0.5 Hz sinusoidal command. 39

Fig. 4-8. Tracking performance of the sliding mode controller corresponding to a 1.0 Hz sinusoidal command. 39

Fig. 4-9. Tracking performance of the sliding mode controller corresponding to a 1.5 Hz sinusoidal command. 40

Fig. 4-10. Tracking performance of the sliding mode controller corresponding to a 2.0 Hz sinusoidal command. 40

Fig. 4-11. Tracking performance of the sliding mode controller corresponding to a band-limited random command..... 41

Fig. 4-12. Tracking performance comparison of the sliding mode controller and the PID/SP combined controller corresponding to a 1.0 Hz sinusoidal command..... 42

Fig. 4-13. Tracking performance comparison of the sliding mode controller and the PID/SP combined controller corresponding to a 2.0 Hz sinusoidal command..... 42

Fig. 5-1. Tracking performance of the sliding mode controller corresponding to a 1.0 Hz sinusoidal command when a 29.5kg mass is loaded. 44

Fig. 5-2. Experimental results of the speed, torque and power input at the pump shaft when the system is tracking a 1.0 Hz Sinusoidal command. 45

Fig. 5-3. Efficiency of system for tracking sinusoidal commands at different frequencies when sliding mode controller is implemented. 46

LIST OF TABLES

Table ..... Page

Table I. Parameters used in the design of pump prototype. 17

Table II. Parameters used in the dynamic model. 36

Table III. Parameters used in the controller. 37

CHAPTER I

INTRODUCTION

This thesis describes the design, modeling, control and efficiency of a variable displacement vane pump based hydraulic actuation system, which is motivated by the need for enhanced efficiency and compactness in mobile hydraulic actuation systems.

Hydraulic actuation systems are widely used in robotics and automation industry. Their popularity is due to the large amount of power that they are able to deliver through small hoses and flexible tubes. Figure 1-1 shows one of the simplest conventional hydraulic actuation systems that consist of some basic elements such as reservoir, filter, pump, accumulator, hydraulic cylinder and servo-control valve. The force that drives the hydraulic cylinder comes from the pressure in the chambers located at each side of the piston. For controlling the motion of the cylinder, the most common practice is to pump the hydraulic fluid into the circuit from the reservoir, and then to control the fluid flow going into one side of the hydraulic cylinder chambers using an assembly of a pressurized accumulator and a proportional servo-valve, meanwhile the fluid in the other cylinder chamber will return to the reservoir through the valve and the returning line and be ready to be pumped again. In hydraulic systems, valves are playing the role of pressure controlled resistor elements that are fundamental energy dissipative parts that cause pressure drop or energy dissipation. It is favorable to remove them from the system for the goal of achieving efficiency.

Among the hydraulic actuation systems used in mobile machines, most of them incorporate

position-controlled hydraulic actuators that utilize an internal combustion (IC) engine (i.e., an essentially constant speed shaft) as the source of driving force of the hydraulic pump. Such systems have found considerably less use in human-scale and sub-human-scale applications (e.g., legged robots), in part because the inefficiency of valve throttling taxes the limited power supply in such systems, and since such systems are typically too small to accommodate fluid cooling, heat generated by fluid throttling is not easily managed.

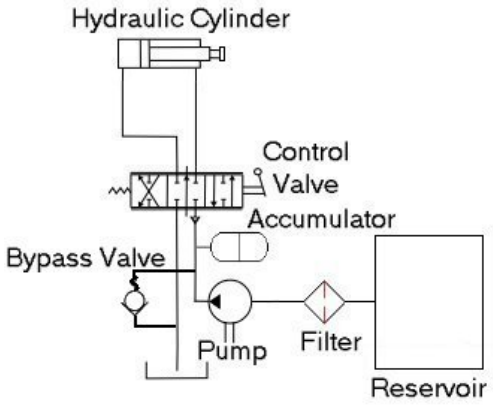

Fig. 1-1. Schematic of a basic hydraulic actuation circuit.

Hydraulic actuators controlled directly by variable displacement pumps (VDP) provide an alternative to valve-controlled hydraulic actuation systems. Rather than controlling flow to a hydraulic actuator via dissipation (i.e. throttling valves), the VDP controls flow via variable displacement, as illustrated in Figure 1-2. Rather than a single pump and one valve per actuator, the VDP approach utilizes a single (smaller) pump for each axis. Unlike valve control, which is fundamentally dissipative, VDP control is theoretically isenergic (i.e., energetically conservative), and therefore provides the potential to achieve a significantly improved efficiency.

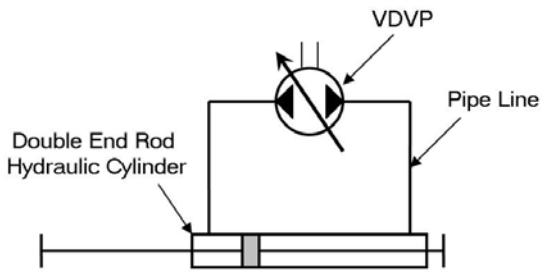

Fig. 1-2. Schematic of a VDP-controlled hydraulic actuator.

Pump-based flow control for a hydraulic actuation system can either be provided by a fixed-displacement pump with a bi-directional variable-speed shaft input, or by a bi-directional variable-displacement pump with a (roughly) constant-speed shaft input. The former approach, often referred to as an electrohydrostatic actuator (EHA), typically utilizes a servo-controlled electric motor to drive the pump, which provides high-bandwidth bidirectional shaft input to drive a bi-directional, fixed displacement pump (e.g., a gear pump). Recent work related to this approach is described in Habibi, Fales, Perron et al. [1-7]. Habibi et al have proved that hydrostatic actuation systems are able to manipulate heavy loads with submicron precision and a large stroke through experiments based on a gear pump and a variable speed motor drive [1-3], who have also proposed a state estimation strategy referred to as the smooth variable structure filter (SVSF) and applied it to their EHA system. Based on the same system used by Habibi, Sampson et al [4] have demonstrated through experiments that due to the nonlinear friction present in the actuator, the utilization of a conventional proportional or PI controller is not sufficient to effectively deal with flow and force disturbances, however, a nonlinear proportional outer-loop controller does result in a substantial performance improvement in

regards to disturbance rejection for positional accuracy. To achieve high regulation rate or short settling time with robust stability, Wang, S. et al [5] proposed a variable structure filter and sliding mode control combined estimation and control strategy for the EHA introduced in [1-3]. Fales et al [6] designed an H-infinity two degrees-of-freedom controller for pump pressure control based on a variable-displacement swash-plate hydraulic pump and performed simulations. Perron et al. proposed a sliding-mode control of an EHA system in a position control application and performed simulations [7].

The primary drawback to the EHA approach proposed by the prior work is the need for an electric servomotor for each axis. Since these servomotors must be rated for the same (or slightly greater) output power as the hydraulic actuator that they supply, and since the continuous output power density of an electric motor is considerably less than the hydraulic actuator, the addition of the electric motor compromises significantly the power density of the hydraulic system. Alternatively, a relatively constant-speed unidirectional shaft input, such as that from an IC engine, can be utilized to drive a controllable bi-directional variable-displacement pump. Considerably less work is published on this topic. Grabbel and Ivantysynova describe the use of this approach via modulation of a swash-plate pumps for large-scale machines [8], and conclude that such an approach can provide a bandwidth that is “competitive” with valve-controlled systems.

This thesis describes the design of a small-scale bi-directional variable-displacement vane pump (i.e., appropriate for human-scale machines) for the purpose of valve-less control of a hydraulic actuation system, which provides bi-directional controlled fluid flow that is capable of performing throttle-less hydraulic servo-actuation with high efficiency when a constant speed is assumed at the

pump input shaft. The fabricated design is experimentally characterized, and both of linear and nonlinear model-based controllers are designed for control of actuator motion tracking after the system dynamics modeling is performed. The controllers are implemented on a single-degree-of-freedom system, and motion tracking is demonstrated and results are compared, which indicate the performance of the controllers. The efficiency of the proposed system is characterized and measured through experiments to demonstrate its potential in energy conservation.

CHAPTER II

DESIGN OF VARIABLE DISPLACEMENT VANE PUMP

Descriptions

The proposed variable displacement vane pump (VDVP) is a variation on a standard rotary vane pump. As a positive-displacement pump, either fixed or variable displacement, a rotary vane pump consists of vanes mounted to a rotor that rotates inside of a stator chamber. Figure 2-1 displays a schematic of the basic working mechanism of the proposed VDVP. There is a particular type of VDVP used in automotive applications such as power steering and automatic transmission which consists of a circular cam that pivots about a point fixed respect to the housing [9-11]. Karmel used to develop the dynamic model of this type of VDVP and analyzed its internal forces [12-13]. Unlike the VDVP studied by Karmel, however, the variable displacement of the proposed VDVP is achieved by the movement of a vertically movable stator that is being driven by a force applied in the vertical direction. With rotor spinning clock wise at all times, the stator is pushed down and comes into contact with the edge of the rotor, as it is shown in Figure 2-1(a). Both of the outside of the rotor and the inside of the stator are circular in shape, but the centers of these two are offset, which cause an eccentricity. All of the vanes can slide into and out of the rotor within their slots and seal on all edges, which create enclosed chambers between every two adjacent vanes that perform the pumping work by delivering liquid from the inlet port to the outlet. The intake side in Case 1 is the right side, with vane chamber volume keeping increasing when it travels from 0^o to 180^o with respect to rotor angle. After passing

180^o, the vane chamber enters the discharge side, which is the left side in Case 1, with chamber volume keeping decreasing when it is sweeping through from 180^o to 360^o. In Case 2, intake and discharge ports are switched when the direction of flow reverses, with the variable stator being pushed all way up. Therefore, with the rotor spinning at a constant speed, the flow rate and the direction of hydraulic flow can be changed by varying the displacement of the stator.

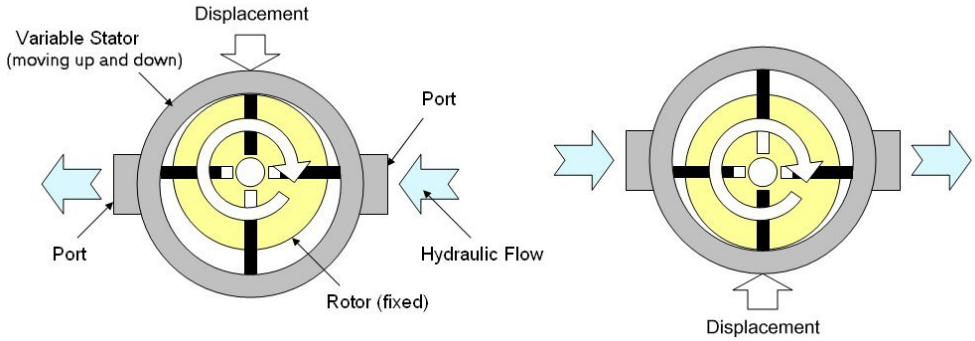

(a). Case 1: stator all way down. (b). Case 2: stator all way up.

Fig. 2-1. Basic mechanism of a variable displacement vane pump.

The physical embodiment of the VDVP is shown in Figure 2-2, which has a DC motor mounted on its top. An exploded view of the embodiment of the VDVP showing all of its mechanical parts is displayed in Figure 2-3. In the design, the rotor includes four vanes and the stator consists of a graphite ring, which is displaced (as illustrated in Figure 2-1) between a pair of graphite end plates via a small electric servomotor and lead screw assembly, as shown in Figure. 2-4 and 2-5. Note that the pump shaft includes a standard pump shaft seal, and all other sealing surfaces utilize either o-ring seals (e.g., between the two halves of the pump body) or cup seals (e.g., on the lead screw shaft), as

they are shown in Figure 2-6.

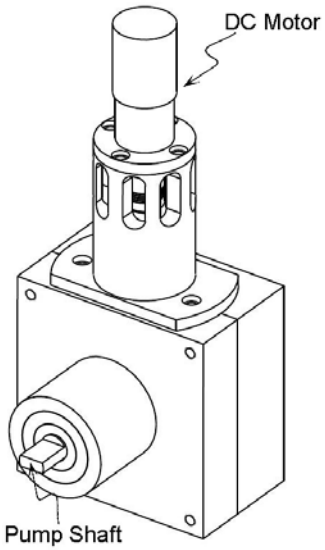

Fig. 2-2. The assembled view of the VDVP.

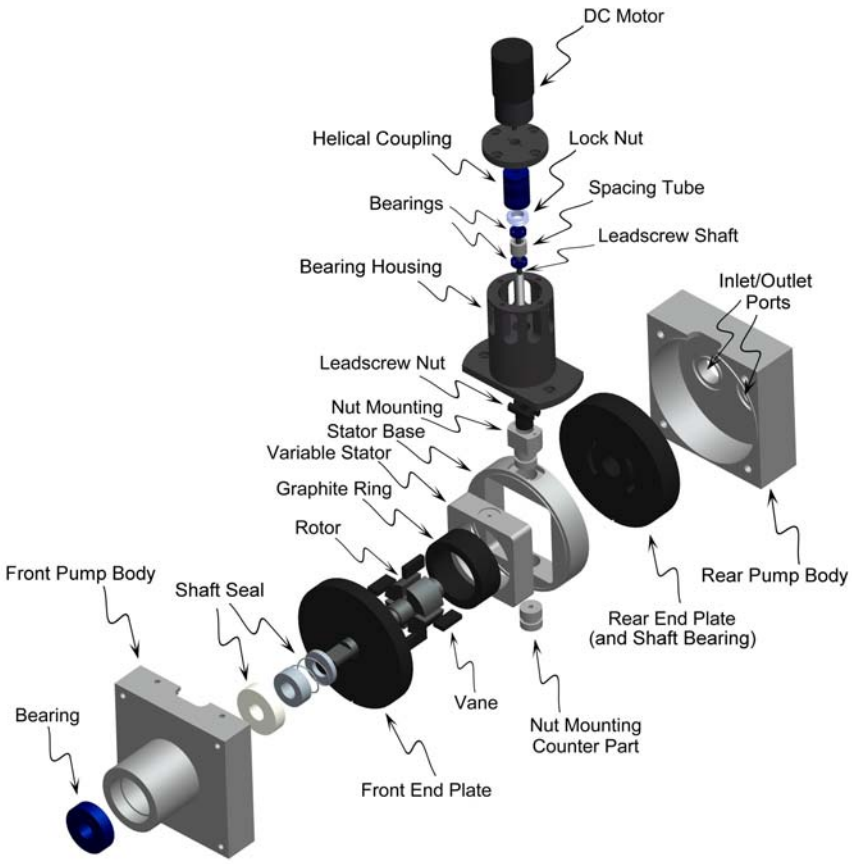

Fig. 2-3. The exploded view with all the mechanical parts of VDVP.

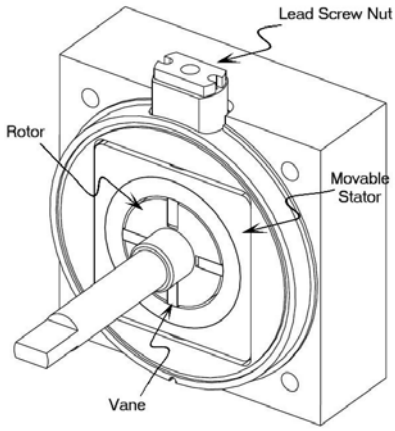

Fig. 2-4. The VDVP with the front half of pump body removed.

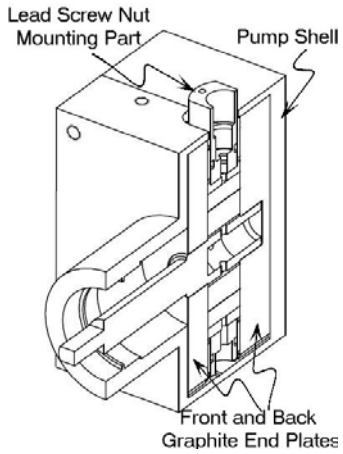

Fig. 2-5. A section view of the VDVP.

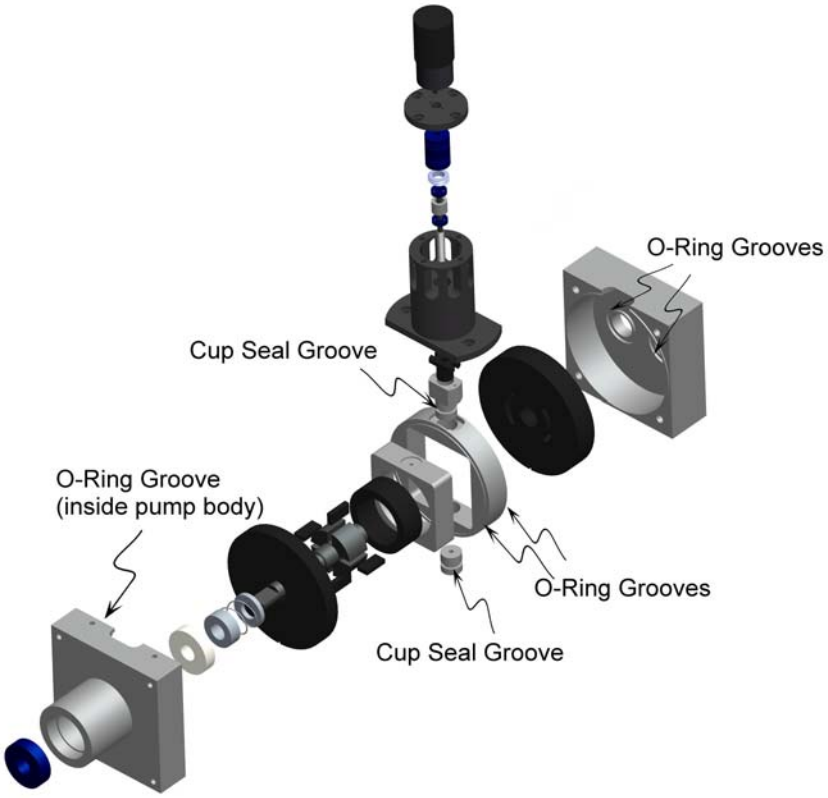

Fig. 2-6. The exploded view that shows the seals of VDVP.

Note that opposing vane slots, shown in Figure 2-7, communicate via small holes, in which

push rods are located, in order to maintain contact between the vane tips and the graphite stator ring. Figure 2-8 shows a front view of the graphite rear end plate, showing the arrangement of the inlet/outlet ports. Each of the inlet/outlet ports spans 90^{o}, which maximizes the intake and discharge regions, prevents flow between these two regions, and also precludes compression or expansion of the incompressible fluid while moving with the rotor. Finally, Figure 2-9 shows a sectional view of the lead screw housing and lead screw. The lead screw nut is affixed to the stator, and thus moves up and down when the lead screw is rotationally driven by the DC servomotor. The total displacement of the stator ring is approximately ±0.7mm. Finally, it should be noted that, since nearly all human-scale applications that would benefit from the proposed approach are multi-axis machines, the VDVP was designed so that several pumps could be stacked together, as shown in Fig. 2-10, to provide compact multi-axis control from a single drive shaft.

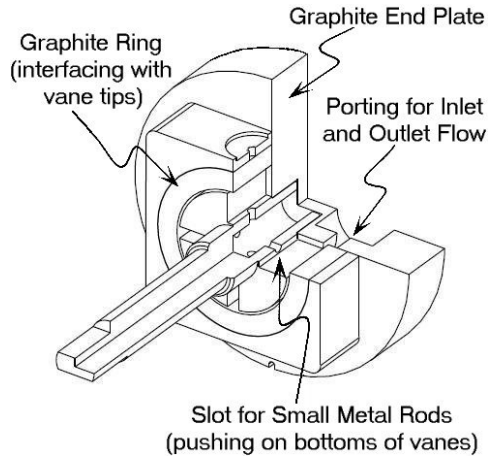

Fig. 2-7. Slots for push rods in VDVP.

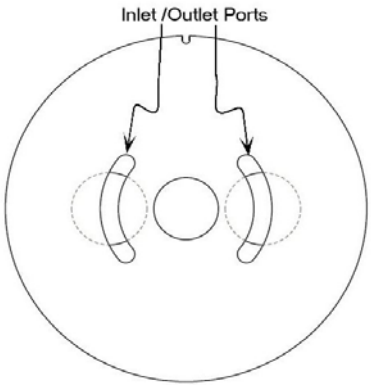

Fig. 2-8. Graphite rear end plate.

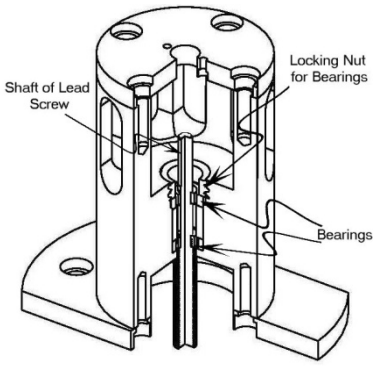

Fig. 2-9. Bearing assembly for lead screw.

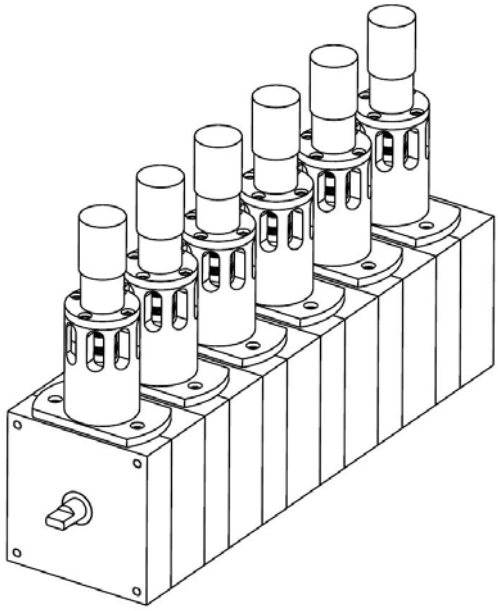

Fig. 2-10. Stack of six variable displacement vane pumps for actuation of a six-axis machine.

Flow Rate Calculation and Sizing

In order to estimate the performance of the VDVP in the design, relationship between pump geometry and pump flow rate has to be developed. A schematic of the cross-section of the VDVP is shown in Figure 2-11 and Figure 2-12, with the center of the fixed rotor above and below the center of the movable stator respectively.

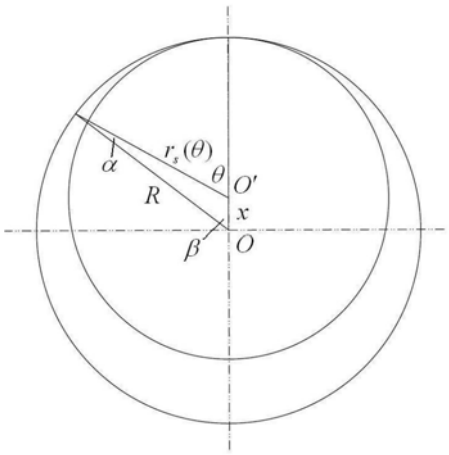

Fig. 2-11. Schematic of cross-section when $x \geq 0$.

As shown in Figures 2-11 and 2-12, R is the radius of the inner surface of the stator, r is the outer radius of rotor, θ is the angle that the vane has swept through relative to the initial up-right position, $r_s(\theta)$ is the distance between the rotor center and the stator inner surface, α is the angle between R and $r_s(\theta)$, β is the angle between R and the vertical center line, and x is the offset between centers O and O'.

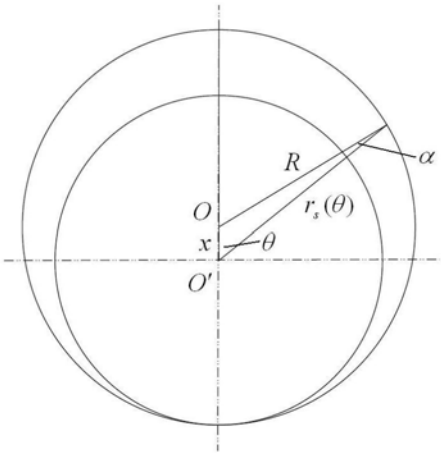

Fig. 2-12. Schematic of cross-section when $x \prec 0$.

The geometry shown on Figure 2-11 can be described by equations in (2-1).

$$\begin{aligned} \sin\alpha &= \frac{x}{R}\sin\theta \\ \beta &= \theta - \alpha \\ r_s^2(\theta) &= R^2 + x^2 - 2Rx\cos\beta \end{aligned} \tag{2-1}$$

Therefore, $r_s(\theta)$ can be expressed by Equation (2-2).

$$r_s^2(\theta) = R^2 + x^2 - 2Rx\cos\left[\theta - \arcsin(\frac{x}{R}\sin\theta)\right] \tag{2-2}$$

If assume that N is the number of vanes of VDVP, then the cross-sectional area between two adjacent vanes can be described by Equation (2-3).

$$\begin{aligned} Area(\theta) &= \int_{\theta-\frac{2\pi}{N}}^{\theta} \frac{1}{2} r_s^2(\theta)d\theta - \frac{\pi r^2}{N} \\ &= \frac{1}{2}\left\{[R^2 + x^2]\theta - 2Rx[A^* + B^*]\right\}\Big|_{\theta-\frac{2\pi}{N}}^{\theta} - \frac{\pi r^2}{N} \end{aligned} \tag{2-3}$$

Where

$$A^* = \frac{\arcsin(\frac{x}{R}\sin\theta)}{2\frac{x}{R}} + \frac{1}{2}\sin\theta\sqrt{1-(\frac{x}{R}\sin\theta)^2}$$

$$B^* = [\frac{\theta}{2} - \frac{1}{4}\sin(2\theta)]\frac{x}{R}$$

Similarly, the cross-sectional area between two adjacent vanes in Figure 2-12 can be described by Equation (2-4).

$$Area(\theta)' = \int_{\theta-\frac{2\pi}{N}}^{\theta} \frac{1}{2} r_s^2(\theta)d\theta - \frac{\pi r^2}{N} \tag{2-4}$$

where $r_s^2(\theta) = R^2 + x^2 - 2R|x|\cos[180^o - (\theta + \alpha)]$.

If the vanes are taken into account in the area calculation of the cross section, as shown in Figure 2-13, the entire cross-sectional area of vanes in a single vane chamber consists of two parts,

which are half of the area of the preceding vane and half of that of the following vane. These two parts of the area can be described by Equation (2-5). The entire area is thus expressed by Equation (2-6), which is to be subtracted from $Area(\theta)$ or $Area(\theta)'$ when the cross-sectional area of vane chamber is calculated.

$$\begin{aligned} Area_vane1(\theta) &= [r_s(\theta) - r] \cdot \frac{W}{2} \\ Area_vane2(\theta) &= [r_s(\theta - \frac{2\pi}{N})] \cdot \frac{W}{2} \end{aligned} \tag{2-5}$$

$$Area_vane(\theta) = Area_vane1(\theta) + Area_vane2(\theta) \tag{2-6}$$

where W is the width of the vane.

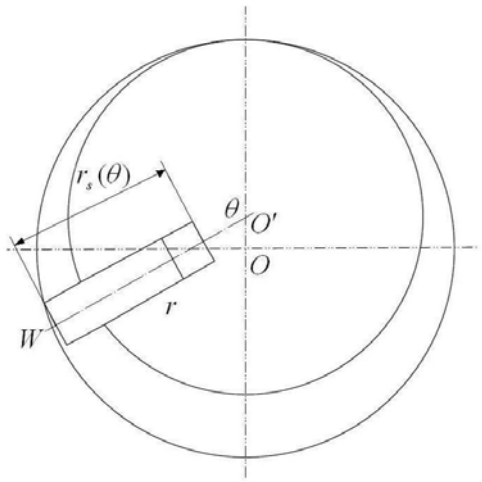

Fig. 2-13. Schematic of cross-sectional area of vane.

Assume that the depth of the stator (or rotor) is L, the angular velocity of rotor is ω, and the proposed pump incorporates four vanes. The maximum volume of the fluid that is delivered by one vane chamber from inlet to outlet port per revolution can be calculated by the difference between

maximum and minimum chamber cross-sectional areas timed by L. When the rotor center is above the stator center, minimum chamber cross-section takes place when θ of the preceding vane is 45^o. When the rotor center is below the stator center, maximum chamber cross-section takes place when θ of the preceding vane is 225^o. Thus the flow rate of the pump Q can be described by Equation (2-7).

$$Q = 4\omega L\left\{[Area(225^o)' - Area_vane(225^o)] - [Area(45^o) - Area_vane(45^o)]\right\} \quad (2\text{-}7)$$

Therefore, depending on the dimension of the hydraulic actuator and the projected working bandwidth, design parameters such as R, r, W, L and x can be decided accordingly using the equations in (2-1) through (2-7). For example, the goal of the first prototype is to drive a hydraulic cylinder of a 1.9 cm (0.75 in) bore and a 10 cm (4 in) stroke at approximately 5 Hz, so the design parameters of the VDVP are chosen according as listed in Table I to meet the demand of the application.

Table I. Parameters used in the design of pump prototype.

Parameter	Description	Value	Unit
R	Inner radius of stator	17	mm
r	Radius of rotor	16	mm
W	Width of vanes	3.3	mm
L	Depth of stator	16	mm
x	Offset of stator	±1.0	mm
ω	Pump speed	1750	RPM

Prototype Performance

The assembled prototype of the VDVP is shown in Figure 2-14. The pump measures 8.5 cm (3.3 in) by 8.5 cm (3.3 in) by 10.4 cm (4 in), and weighs 1.25 kg (2.75 lb). The stator position (and thus the pump displacement) is controlled via a 22 mm diameter DC motor (Maxon model no. 314706) with a 4.4:1 planetary gearhead and an integrated rotary encoder. The stator motion is controlled via a proportional-derivative (PD) controller between the rotary encoder and the motor current (i.e., technically the motor position is being controlled rather than the stator position, although the two are kinematically coupled via the lead screw transmission).

Fig. 2-14. VDVP prototype (with a DC motor assembled).

The stator step response for a command amplitude representing ±50% of the stator motion is shown in Figure 2-15. Figure 2-16 shows the measured bandwidth of the stator motion, also for a command amplitude of ±50%, demonstrating a -3dB bandwidth of approximately 7 Hz. Figure 2-17

shows the measured pump output flow rate (of water) as a function of stator displacement for a shaft input speed of 1750 RPM (which is the shaft speed used in the control experiments described subsequently). Finally, Figure 2-18 shows the measured pump characteristics, at maximum stator displacement (i.e., 0.7 mm), using a working fluid of water, for various input shaft speeds. Note that the maximum pressure is limited by vane leakage, which could presumably be increased by tighter tolerances in fabrication.

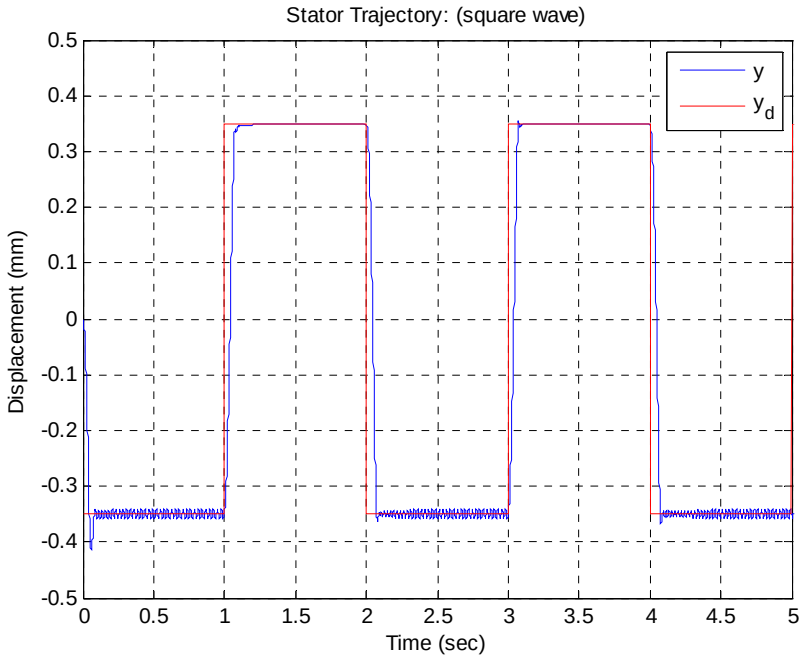

Fig. 2-15. Step response of VDVP stator corresponding to ±50% of the stator motion.

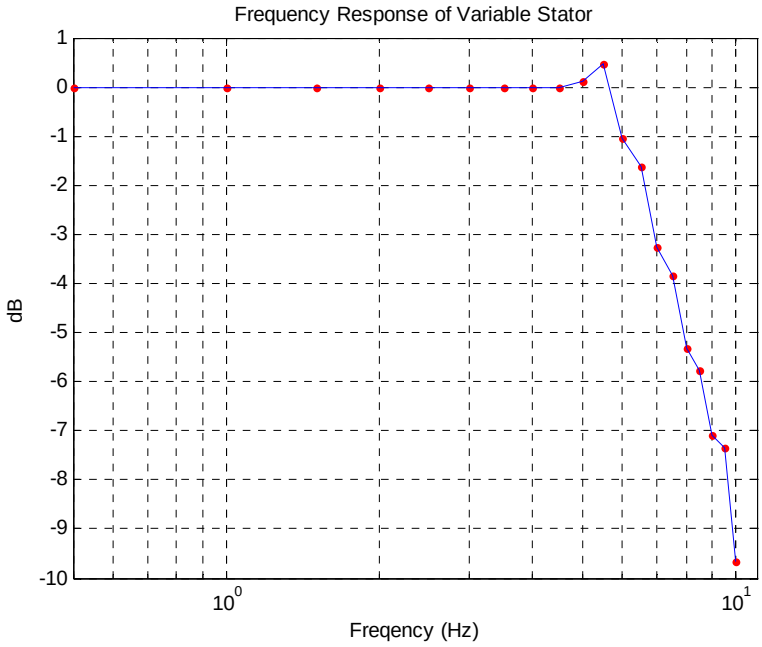

Fig. 2-16. Bandwidth of VDVP stator motion.

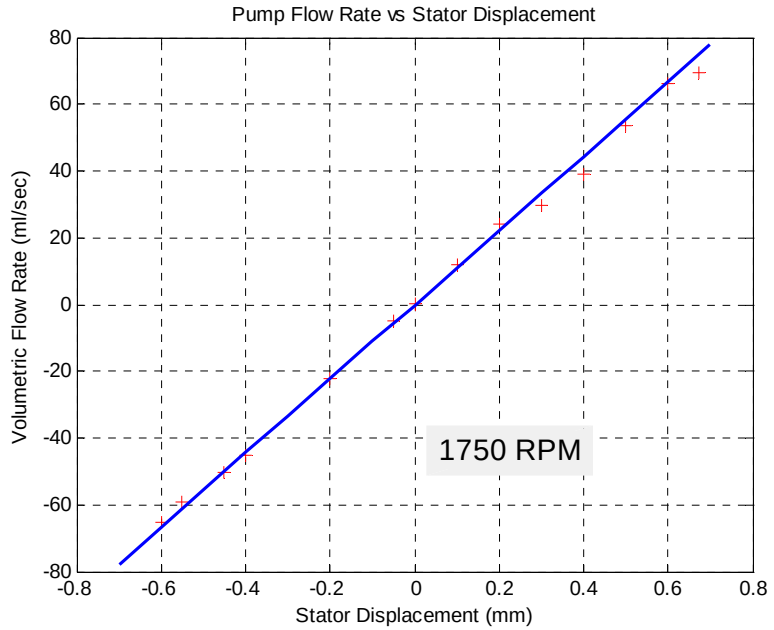

Fig. 2-17. Pump flow rate as a function of stator displacement at a shaft speed of 1750 RPM.

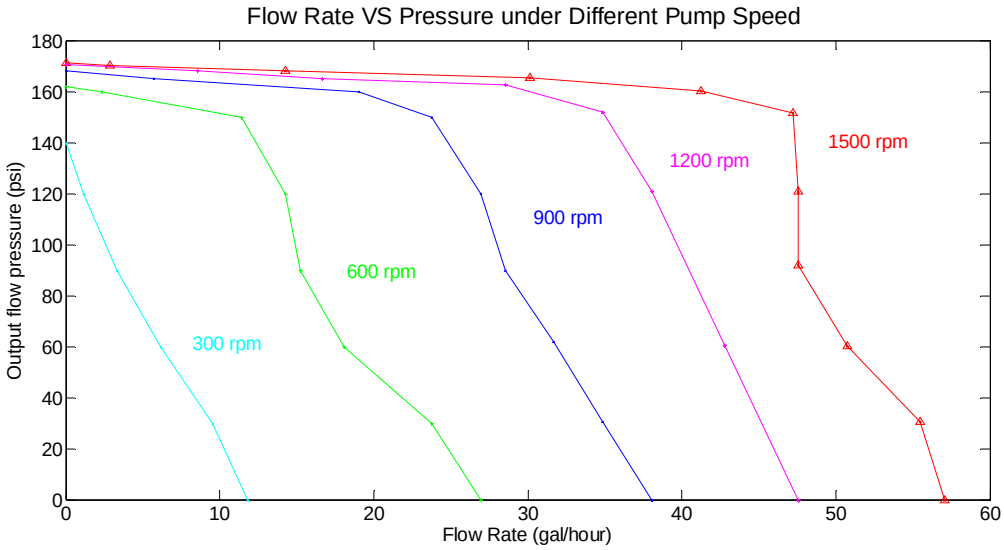

Fig. 2-18. Experimentally determined pump characteristics.

Experimental Setup

The proposed control approaches were implemented on a VDVP-controlled hydraulic actuator, as schematically illustrated in Figure 1-2. The experimental system consisted of the VDVP shown in Figure 2-14, which drives a double acting, double rod hydraulic cylinder (Bimba HL-044-DXDE) with a 1.9 cm (0.75 in) bore and a 10 cm (4 in) stroke, as shown in Figure 2-19, using water as the working fluid. The hydraulic cylinder rod was rigidly attached to a 10 kg mass, which was mounted on a linear slide. Since the proposed controllers requires measurement of the model states, a linear potentiometer (Midori LP-100F) was used to measure the load displacement (from which velocity and acceleration were derived), and a set of pressure sensors (FESTO SDE-16-10V/20mA) were used to measure the cylinder pressures. The controller was implemented at a sampling rate of 1 kHz on a Pentium 4 processor with the real-time interface provided by Matlab/Simulink (The MathWorks, Inc.).

Note that the VDVP is intended to be driven by an IC engine, although for purposes of the experimental setup, it was driven by a DC motor, controlled to drive the pump at a constant shaft angular velocity.

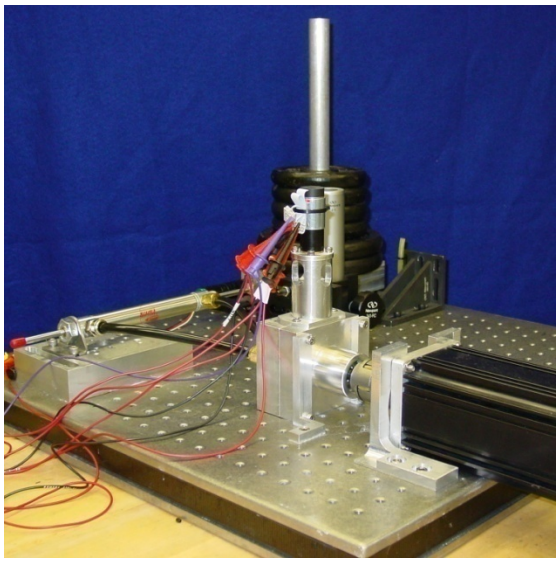

Fig. 2-19. Hydraulic circuit consists of VDVP and hydraulic cylinder.

CHAPTER III

PRELIMINARY CONTROL OF VDVP BASED HYDRAULIC ACTUATION SYSTEM

Linear Model of the VDVP Based Hydraulic Actuation System

In order to control the hydraulic actuation system displayed in Figure 2-19, the dynamics of this system must be known. Under ideal conditions, the VDVP in this system can be viewed as a flow source that pumps fluid from one side of the cylinder into the other side. Equation (3-1) describes the relationship between the flow rate, the cylinder piston speed and the pump displacement.

$$\tilde{q} = A\dot{x} = k_p y \tag{3-1}$$

where $\tilde{q}$ is the flow rate of the VDVP, A is the cross-section area of the cylinder piston, $\dot{x}$ is the speed of the cylinder piston, k_p is the pump constant, and y is the pump displacement. Therefore, the open loop transfer function (TF) of the system under ideal conditions is described by equation (3-2).

$$G(s) = \frac{X(s)}{Y(s)} = \frac{k_p}{A} \cdot \frac{1}{s} = \frac{K'}{s} \tag{3-2}$$

where K' is a constant that equals to $\frac{k_p}{A}$.

However, with the effects of the air bubbles existing in the circuit, the compliance of the flexible tubing, and the Coulomb friction between the cylinder rods and the seals, the condition of the experiment system is far from being ideal. Therefore, the TF described by (3-2) will not apply, and it

can only tell part of the truth of the system. The TF of the system is then chosen to be determined experimentally. The system's open loop responses to Sinusoidal signals ranging from 0.1 Hz to 10 Hz are collected. And the frequency response is plotted and analyzed in the Bode diagrams in Figure 3-1. The dots in red color are data points obtained from experiments, the curve in blue colored solid line is the estimated TF of the system without time delay, and the curve in green colored dashed line is the estimated TF of the system that has time delay.

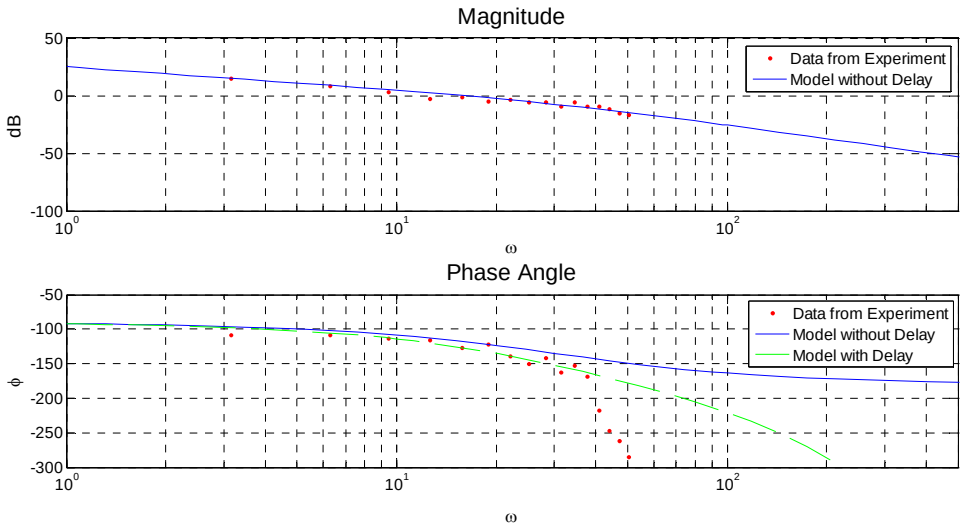

Fig. 3-1. Experimentally determine the system transfer function.

Based on the information shown in both of the magnitude plot and the phase plot, the estimated TF of the system is a second order system with a phase lag (time delay), which can be described by equation (3-3).

$$G'(s) = \frac{X(s)}{Y(s)} = \frac{540 \cdot e^{-0.01 \cdot s}}{s(s+30)} \tag{3-3}$$

PID and Smith Predictor Combined Controller Design

A control scheme combined with a Smith Predictor (SP) and a PID controller is adopted to control this system, the former is known for being effective in controlling systems that have time delay [14]. Figure 3-2 shows a diagram of the controller with SP and PID. $C_0(s)$ is a standard PID controller, $P(s)$ is the plant, $\hat{P}_0(s)$ is the nominal TF of the plant that is without the time delay, and $\hat{P}(s)$ is the nominal TF with delay.

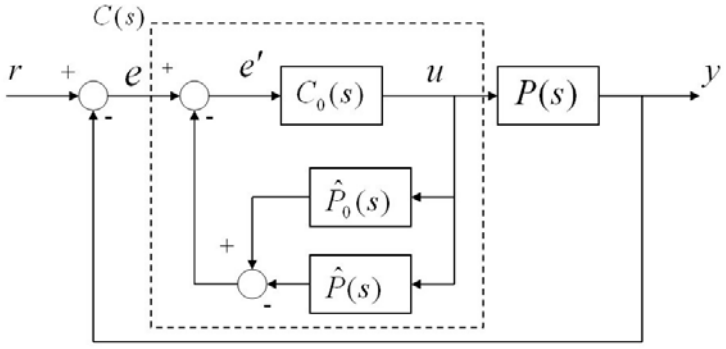

Fig. 3-2. Smith Predictor.

Experimental Results

The controller shown in Figure 3-2 is implemented in the experimental setup and tuned to do a series of position tracking. Figure 3-3 shows the tracking of a step signal.

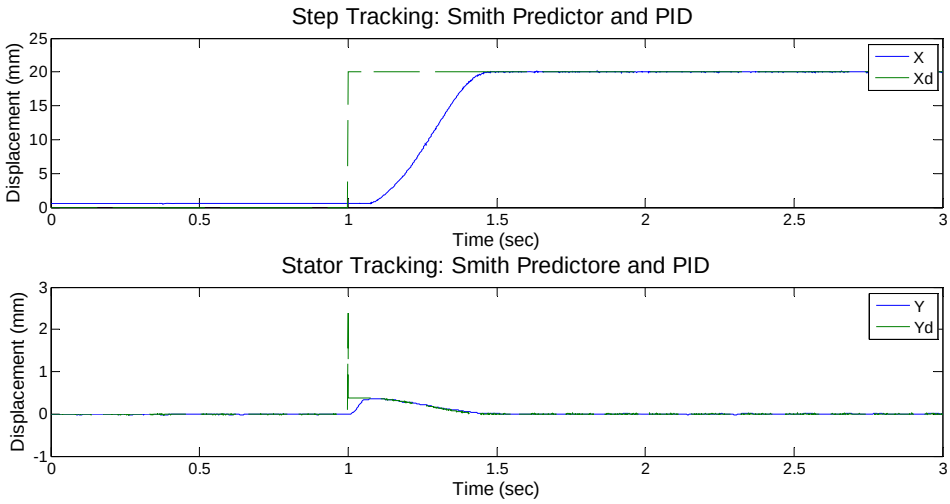

Fig. 3-3. SP and PID: Step tracking.

Figure 3-4, Figure 3-5, Figure 3-6 and Figure 3-7 show the tracking of Sinusoidal signals, which frequencies are 0.25 Hz, 0.5 Hz, 1.0 Hz and 2.0 Hz.

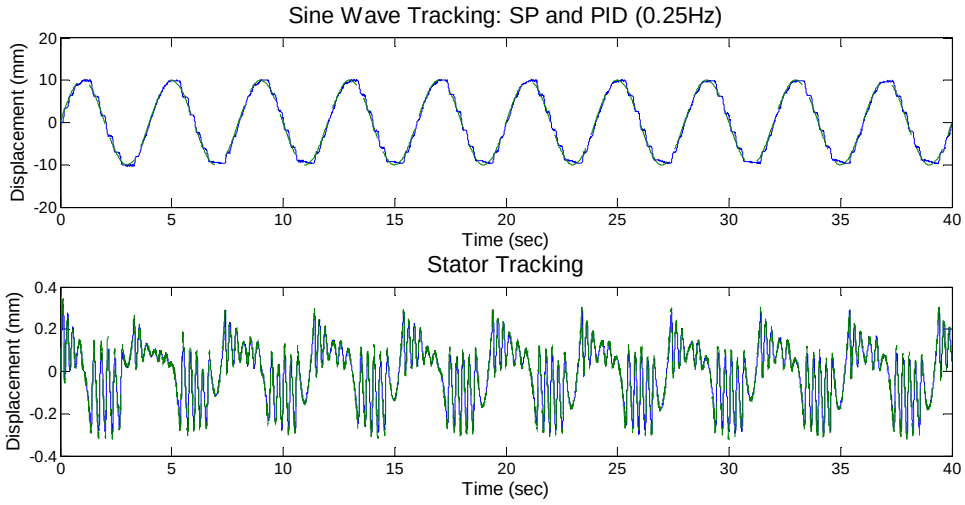

Fig. 3-4. SP and PID: Sinusoidal signal tracking, 0.25 Hz.

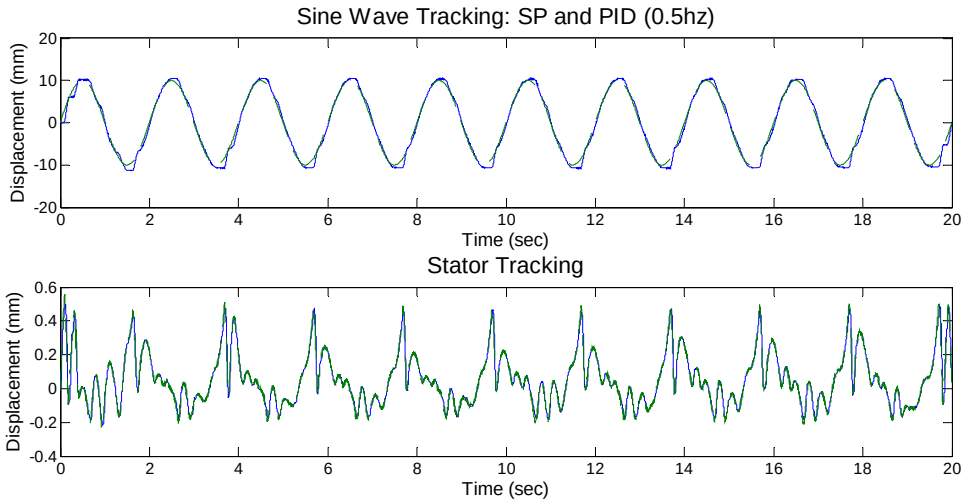

Fig. 3-5. SP and PID: Sinusoidal signal tracking, 0.5 Hz.

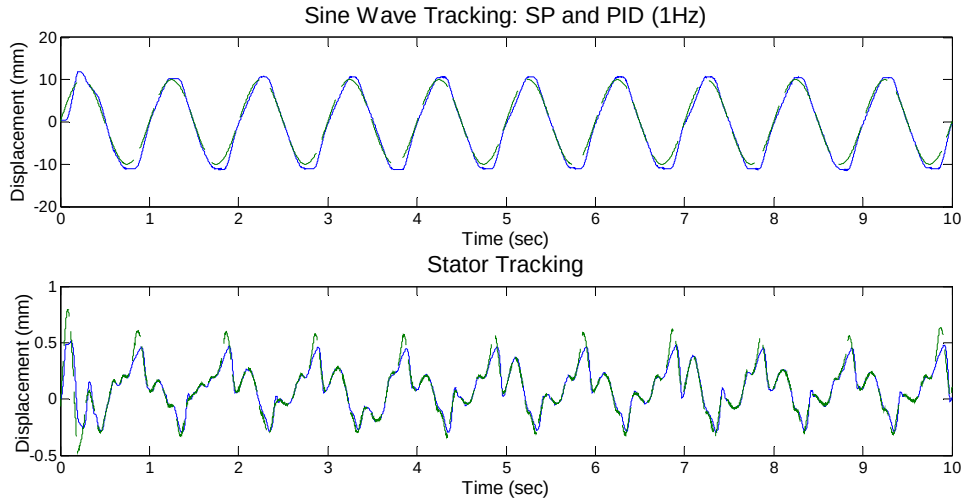

Fig. 3-6. SP and PID: Sinusoidal signal tracking, 1 Hz.

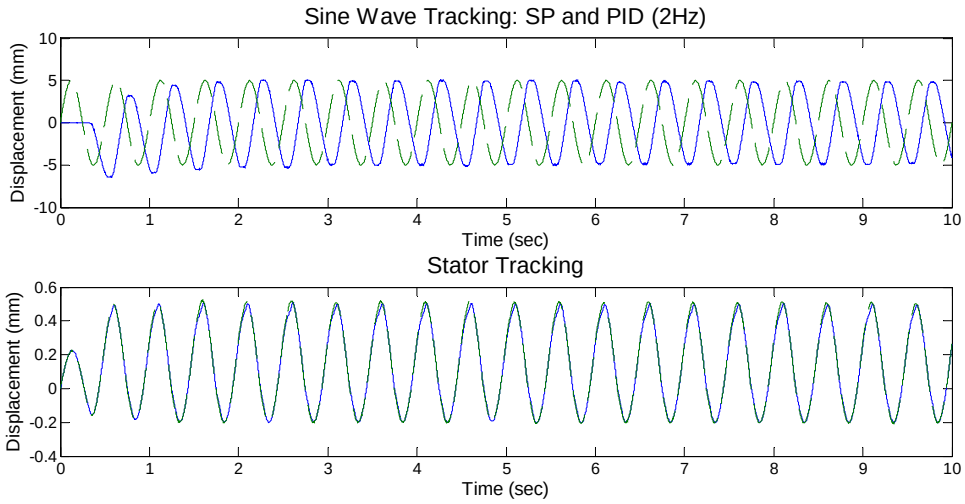

Fig. 3-7. SP and PID: Sinusoidal signal tracking, 2 Hz.

Figure 3-8 shows a comparison of the tracking of a 1 Hz Sine wave using different controllers, the left one is using a PID controller only, and the right one is using a combination of SP and PID. The variance in respect to the reference signal is 1.8718 in the left system, while the value becomes 1.5373 in the right one. In another word, the tracking performance is improved by 18% as far as variance is concerned when the combination of SP and PID is applied for the controller in the tracking of a 1 Hz Sinusoidal wave.

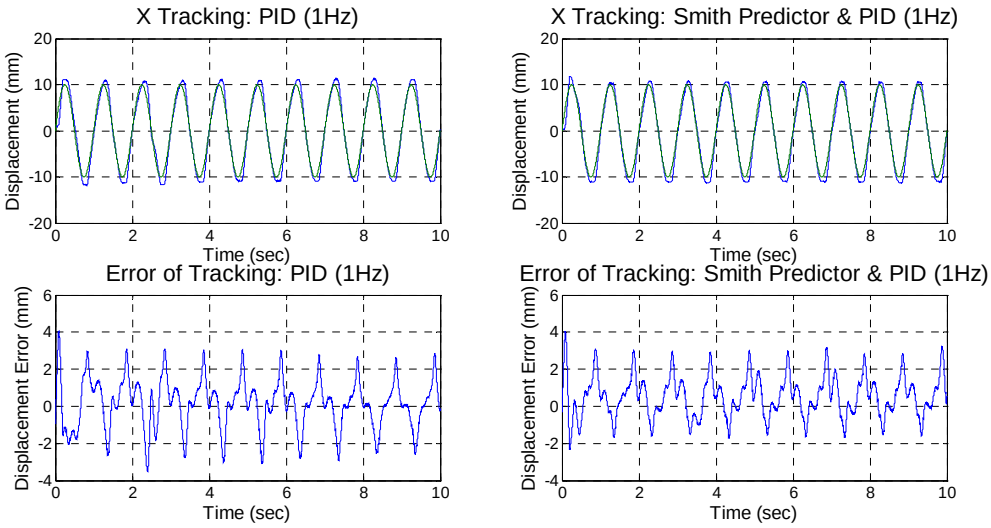

Fig. 3-8. Compare tracking performance between using PID controller only and using SP&PID controller.

Experimental results show that the application of an SP and PID combination controller has a better performance than applying a PID controller only. Control performance is satisfactory when the frequency of the reference signal is below 2 Hz. The preliminary control is performed based on a simplified and linearized model that is experimentally determined, lacking of the information of two important states, the pressures in each side of the hydraulic cylinder, so this model is not precisely describing the dynamics of the system. Therefore, to achieve good control performance in higher bandwidth, a more accurate model and a more sophisticated controller have to be developed.

CHAPTER IV

ADVANCED CONTROL OF VDVP BASED HYDRAULIC ACTUATION SYSTEM

Nonlinear Model of the VDVP Based Hydraulic Actuation System

The model for the VDVP-controlled hydraulic actuator is similar to the standard model used for other hydraulic actuators, but the flow rate of fluid entering the cylinder is a function of the pump displacement rather than valve spool displacement. Figure 4-1 shows a hydraulic power cylinder that is driven by the VDVP. P_a and P_b are pressures in chambers A and B. x is the position of the piston. a is the area of surface on side A and B. m is the mass of the piston. Q_a and Q_b are the fluid flow rate in A and B. f is the external force applied on the piston, specifically Coulomb friction f_c.

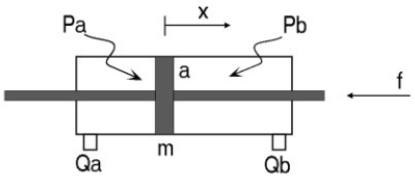

Fig. 4-1. Schematic of a hydraulic cylinder.

Assume that the hydraulic cylinder shown in Figure 4-1 has an inertial and viscous load, its dynamics can be described by equation (4-1).

$$P_a a - P_b a - f_c = m\ddot{x} + b_p \dot{x} \tag{4-1}$$

Differentiation of (4-1) with respect to time gives (4-2). The Coulomb friction f_c in the system is neglected and is therefore r moved from the dynamic model.

$$\begin{aligned} &\dot{P}_a a - \dot{P}_b a = m\dddot{x} + b_p \\ &\ddot{x} = \frac{1}{m}[\dot{P}_a a - \dot{P}_b a - b_p \dot{x}]\dot{x} \end{aligned} \tag{4-2}$$

The hydraulic fluid in cylinder chambers can be considered as a mixture of liquid and a small amount of entrained, non-dissolved gas. Applying the continuity equation, the rate of change of the pressure in chamber A and B can be expressed as the following equations in (4-3).

$$\begin{aligned} \dot{P}_a &= \frac{B_k}{V_a}[Q_a - a\dot{x}] \\ \dot{P}_b &= \frac{B_k}{V_b}[Q_b + a\dot{x}] \end{aligned} \tag{4-3}$$

in which B_k is the bulk modulus of the hydraulic fluid, V_a and V_b are volume of chambers A and B.

The flow rate of each chamber is described by equation (4-4), where k_p is the pump constant, y is the displacement of the variable stator, and L_f is the leakage factor of the pump, which is set to zero to simplify the dynamic model.

$$\begin{aligned} Q_a &= k_p y - L_f (P_a - P_b) \\ Q_b &= -Q_a \end{aligned} \tag{4-4}$$

Substituting (4-3) and (4-4) into (4-2) gives (4-5),

$$\ddot{x} = -\frac{1}{m}[B_k a^2 (\frac{1}{V_a} + \frac{1}{V_b})\dot{x} + \dot{f}_c + b_p \ddot{x}] + \frac{B_k K_p a}{m}[\frac{1}{V_a} + \frac{1}{V_b}]y \tag{4-5}$$

where $V_a = V_{a0} + ax$

$$V_b = V_{b0} - ax$$

Equation (4-5) gives the system dynamic model relating the pump displacement y as the input to the load position x as the output, where $\ddot{x}$ is completely controlled by the displacement y of the variable stator. Equation (4-5) can be written in a general form as described by equation (4-6).

$$\ddot{x} = f + bu \tag{4-6}$$

where $f = -\frac{1}{m}[B_k a^2(\frac{1}{V_a} + \frac{1}{V_b})\dot{x} + \dot{f}_c + b_p\ddot{x}]$

$$b = \frac{B_k K_p a}{m}[\frac{1}{V_a} + \frac{1}{V_b}]$$

$$u = y$$

Identification of Model Parameters

In order to determine the unknown parameters in the dynamic model described by (4-6), which are B_k, k_p and b_p, experiments are performed and their results are treated in computer with using Matlab/System Identification Toolbox. Since the leakage factor L_f is set to zero and is removed from the dynamic model described by (4-6), so it is not measured in the system identification process. In the experiments, the system are given a series of square wave inputs, and its outputs are recorded and processed in Matlab, which provides a function that basically utilizes the prediction error method (PEM) in system identification. A schematic diagram of the PEM is displayed in Figure 4-2, where $u(t)$, $y(t)$ and $v_0(t)$ are input, output and disturbance of the system, $\hat{y}(t,\theta)$ is the

predicted estimate of the output $y(t)$, $\hat{\theta}$ is the estimated parameters, $\varepsilon(t,\theta)$ is the prediction error, and $V_N(\theta) = \sum_{t=1}^{N} \varepsilon^2(t,\theta)$ is the cost function to be minimized for optimal estimation of $\hat{\theta}$.

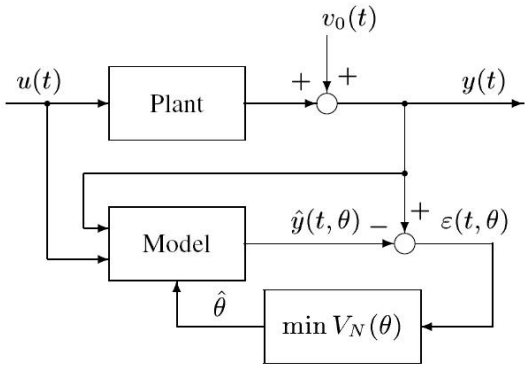

Fig. 4-2. Prediction error method.

To explain the parameter estimation procedure, one group of the experiment data is displayed in Figure 4-3, showing the input and output of the system. A segment of data from 2 to 5 second from the experiment is used in the identification process, and $\hat{y}(t,\theta)$ based on the estimated parameters is plotted together with the original experimental result in Figure 4-3. Then another segment of data from experiment, the input command to system, from 6 to 8 second is used in the dynamic model (with estimated parameters plugged in) to generate the predicted system output, which is plotted together with that of the experimental result, shown in Figure 4-4, to validate the parameter estimation. After performing a few iterations of this process with updated parameters for each time, the optimal estimates for the unknown parameters are determined and applied to the dynamic model, as listed in Table II. Note that the random-frequency square wave input with used here is not the standard input

usually adopted in system identification for a nonlinear system. The ideal input would typically be a band-limited random signal that is rich in both of frequency and magnitude. The current input has been adopted because it can avoid the slide from hitting the boundary of motion in the experimental setup, which is a problem the experiment was running into when the more desirable band-limited random signal was used as system input.

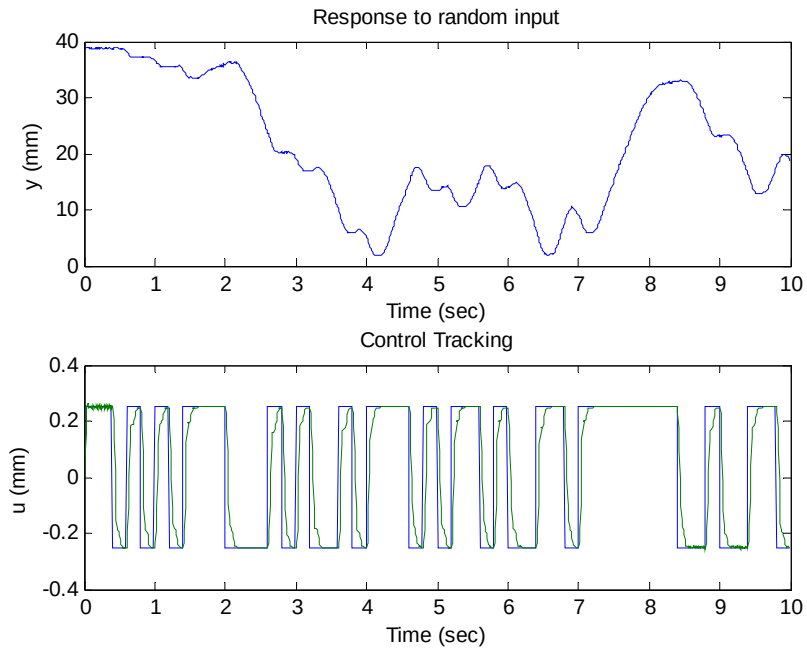

Fig. 4-3. Experimental results in system identification.

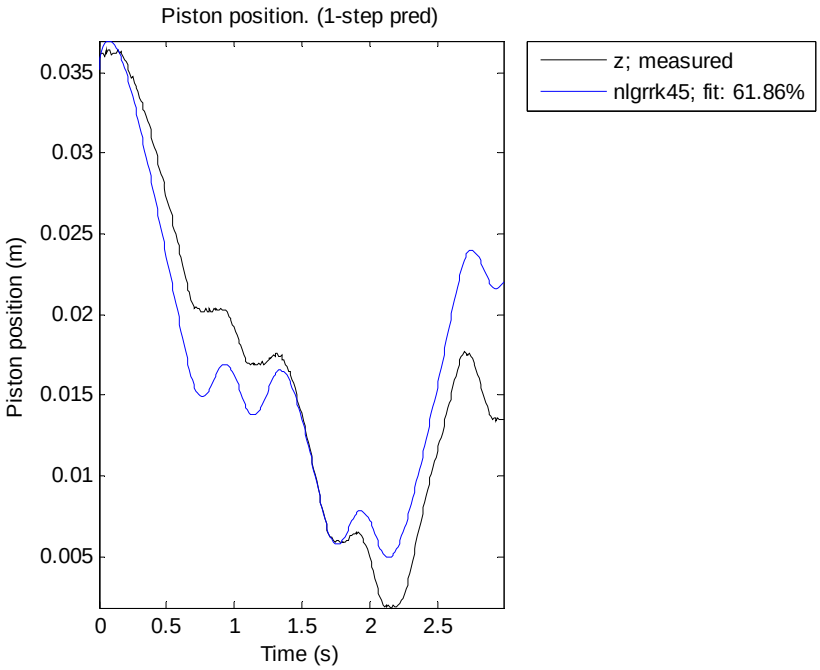

Fig. 4-4. Parameter estimation with experimental results.

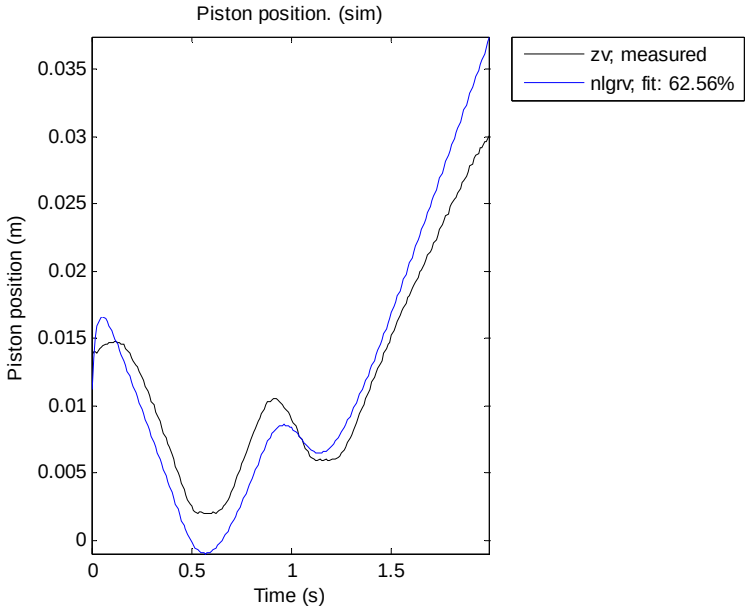

Fig. 4-5. Model validation based on the estimated parameters and experimental results.

Table II. Parameters used in the dynamic model.

Parameter	Description	Value	Unit
b_p	Damping coefficient	400	N-m
k_p	Pump constant	0.085	m^2/s
B_k	Bulk modulus	700	kPa

Sliding Mode Control Design

The control canonical model given (4-6) is well suited to a sliding mode control approach, which is a major robust control approach to dealing with model parameter inaccuracies. In order to ameliorate the Coulomb friction assumed to be present in the cylinder seals, an integral sliding surface is used, defined for the third-order dynamics as:

$$s = (\frac{d}{dt} + \lambda)^3 \int_0^t e d\tau \tag{4-7}$$

where $e = x - x_d$, x_d is the desired position and λ is the control gain. The corresponding sliding condition is:

$$\frac{1}{2}\frac{d}{dt}s^2 \le -\eta|s| \tag{4-8}$$

where η is a positive constant.

Equation (4-7) can be expressed by equation (4-9),

$$
\begin{aligned}
s &= (\frac{d^3}{dt^3} + \lambda^3 + 3\frac{d^2}{dt^2}\lambda + 3\frac{d}{dt}\lambda^2)\int_0^t e d\tau \\
&= \ddot{e} + 3\lambda\dot{e} + 3\lambda^2 e + \lambda^3 \int_0^t e d\tau
\end{aligned}
\tag{4-9}
$$

Differentiation of (4-9) with respect to time gives (4-10).

$$
\begin{aligned}
\dot{s} &= \dddot{e} + 3\lambda\ddot{e} + 3\lambda^2\dot{e} + \lambda^3 e \\
&= \dddot{x} - \dddot{x}_d + 3\lambda^2\dot{e} + \lambda^3 e \\
&= f + bu - \dddot{x}_d + 3\lambda\ddot{e} + 3\lambda^2\dot{e} + \lambda^3 e
\end{aligned}
\tag{4-10}
$$

Therefore a sliding mode control law is developed as described in [15]:

$$
\hat{u} = \frac{1}{\hat{b}}[\dddot{x}_d - \hat{f} - 3\lambda\ddot{e} - 3\lambda^2\dot{e} - \lambda^3 e - \hat{k}\,\mathrm{sgn}(s)] \tag{4-11}
$$

The model parameters and control gains used in the sliding mode controller are listed in Table III. Note that the control gains were determined by tuning, such that both were as large as possible, without introducing (noticeable) noise into the control command.

Table III. Parameters used in the controller.

Parameter	Description	Value	Unit
a	Piston area	283.5	mm^2
k	Robustness gain	2×10^7	mm/sec^3
λ	Error dynamic gain	19.5	rad/sec
L_f	Leakage factor of pump	0	m^3/Pa-sec
V_{a0}	Initial volume of chamber a	2.7×10^{-5}	m^3
V_{b0}	Initial volume of chamber b	4.2×10^{-5}	m^3

Experimental Results

Experiments were conducted to demonstrate the tracking performance and to compare it with that of a previously applied PID and Smith Predictor (SP) combined controller that is based on a linearized model of the system. Figure 4-6 shows the tracking of a step signal when the proposed sliding mode controlled was implemented.

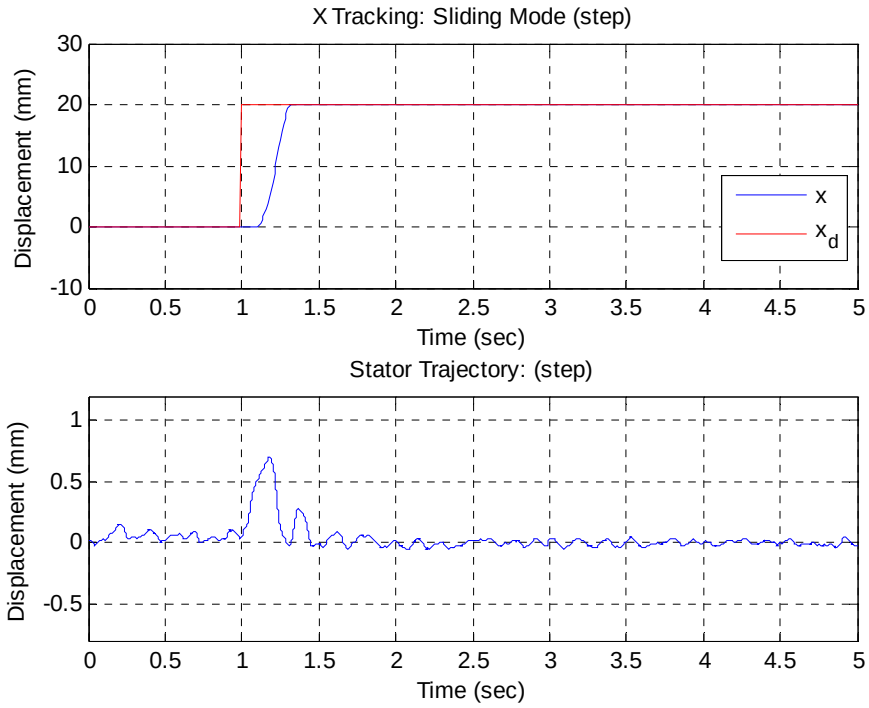

Fig. 4-6. Step tracking of the sliding mode controller.

Figures 4-7 through 4-10 show the tracking of desired sinusoidal position trajectories at different frequencies, such as 0.5 Hz, 1 Hz, 1.5 Hz and 2.0 Hz, when the proposed sliding controller was applied. Figure 4-11 shows the tracking performance of the system corresponding to a band-limited pseudo- random signal. In all cases, the load effectively tracks the respective desired trajectory.

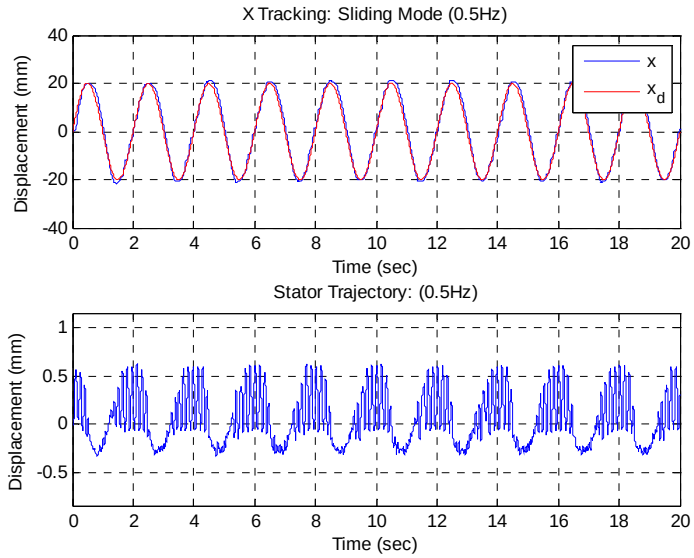

Fig. 4-7. Tracking performance of the sliding mode controller corresponding to a 0.5 Hz sinusoidal command.

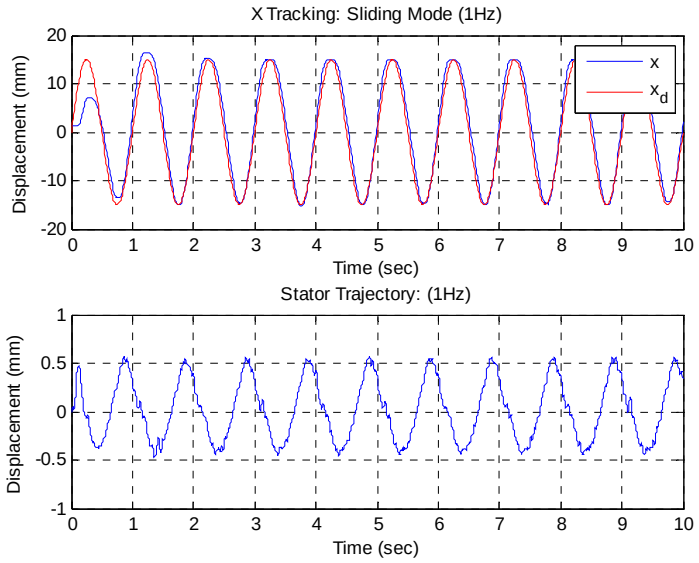

Fig. 4-8. Tracking performance of the sliding mode controller corresponding to a 1.0 Hz sinusoidal command.

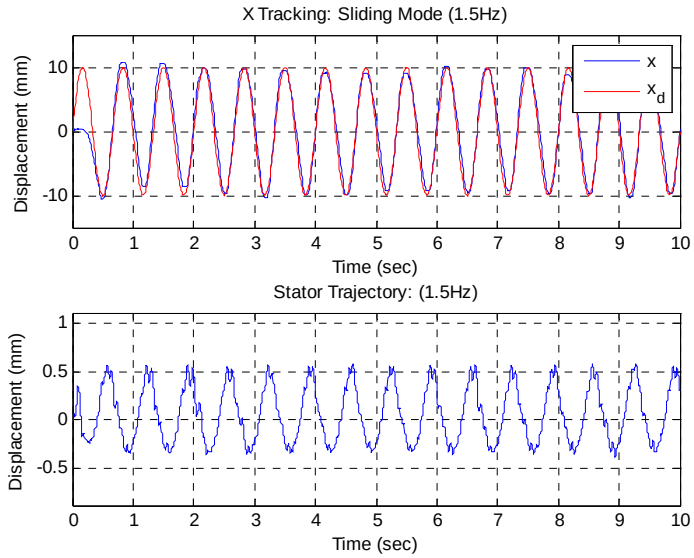

Fig. 4-9. Tracking performance of the sliding mode controller corresponding to a 1.5 Hz sinusoidal command.

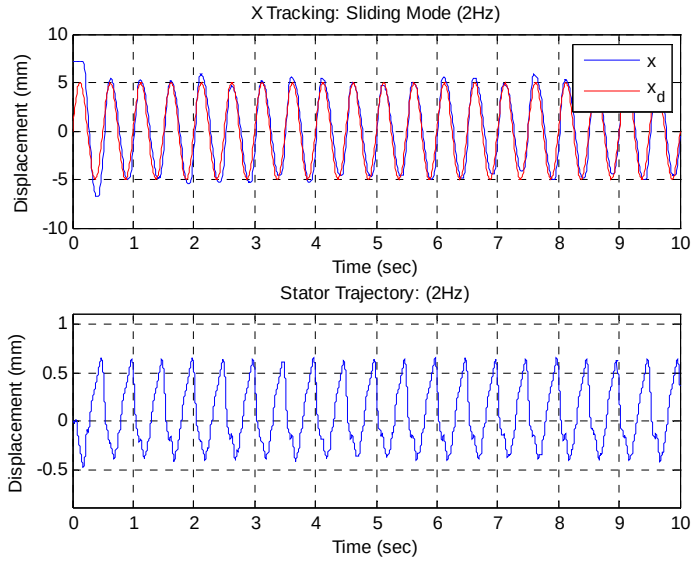

Fig. 4-10. Tracking performance of the sliding mode controller corresponding to a 2.0 Hz sinusoidal command.

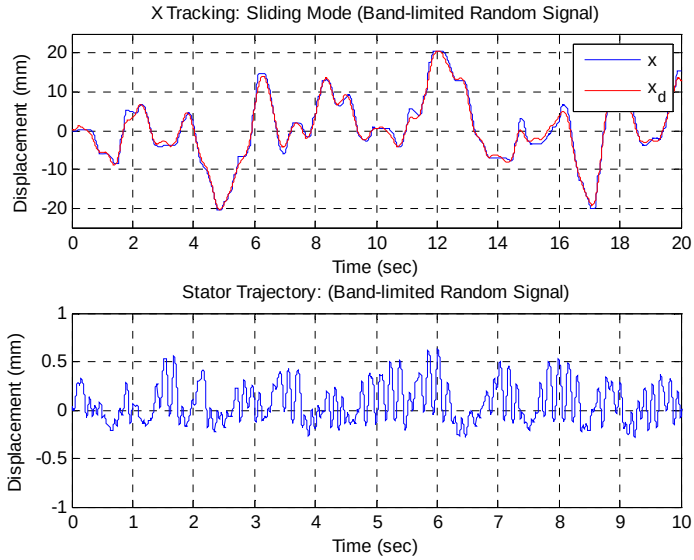

Fig. 4-11. Tracking performance of the sliding mode controller corresponding to a band-limited random command.

Figure 4-12 and Figure 4-13 show a comparison of tracking performance of the proposed sliding mode controller approach to a PID and SP combined controller implemented in a prior work, which indicate that the proposed sliding mode controller provides a better tracking performance in both of magnitude and phase. In Figure 4-12, the standard deviation in respect to the reference command, a 1.0 Hz sinusoidal signal, is 1.2399 for the PID/SP controller, while the standard deviation in respect to the same reference signal is only 0.0020 for the sliding mode controller. In Figure 4-13, in respect to the same reference command given, the standard deviation for the PID/SP controller is 6.1307, while the standard deviation comes down to 0.0013 when the sliding mode controller was applied. It is noted that the control performance was significantly improved by implementing the proposed sliding mode controller.

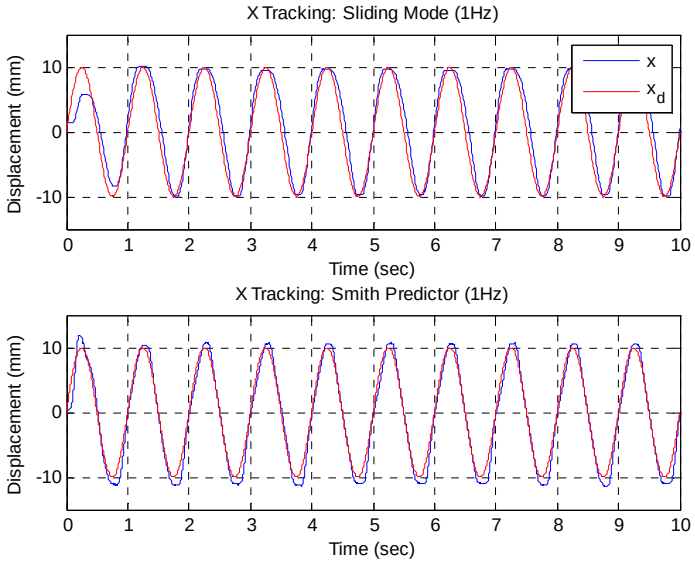

Fig. 4-12. Tracking performance comparison of the sliding mode controller and the PID/SP combined controller corresponding to a 1.0 Hz sinusoidal command.

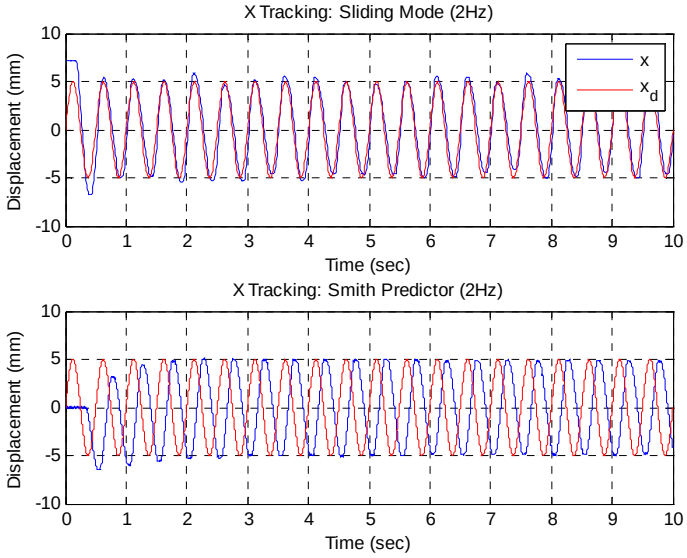

Fig. 4-13. Tracking performance comparison of the sliding mode controller and the PID/SP combined controller corresponding to a 2.0 Hz sinusoidal command.

CHAPTER V

EFFICIENCY OF VDVP BASED HYDRAULIC ACTUATION SYSTEM

The input power of the proposed hydraulic actuation system based on VDVP can be calculated from the speed and torque output of the brushless motor (Aerotech BM500) that is connected to the VDVP's input shaft, as described by equation (5-1).

$$P_{in} = \omega \cdot \tau \tag{5-1}$$

where ω is the output speed of motor in rad/s, τ is the output torque of motor in N-m, and the unit of P_{in} is Watt. Therefore the energy consumption that is input to the system is:

$$E = \int P_{in} dt \tag{5-2}$$

The output power of the system is measured when the hydraulic actuator is driving a mass of 29.5 kg (65 lb) mounted on the slider and tracking a series of desired sinusoidal position trajectories at different frequencies, such as 0.5 Hz, 1.0 Hz, 1.5 Hz and 2.0 Hz. Assume that the trajectory tracked by the hydraulic actuator is $x = A \cdot \sin(2\pi f \cdot t)$, then the work that is done by the actuator can be described by equation (5-3).

$$W = \int F \cdot dx = \int m|a| \cdot d|x| = \int m|\ddot{x}| \cdot d|x| \tag{5-3}$$

where F is the driving force from the actuator, m is the mass of the weights, a is the acceleration of the mass, and x is the displacement of the mass. Note that since the proposed actuation system is a non-conservative system, the absolute values of $\ddot{x}$ and x are used to calculate the total work done by the actuator. Therefore the efficiency of the system can be expressed by

equation (5-4).

$$\eta = \frac{W}{E} \times 100\% \tag{5-4}$$

Figure 5-1 shows the tracking of the sliding mode controller corresponding to a 1.0 Hz sinusoidal command when weights of 29.5kg were loaded on the slide during the experiment of efficiency estimation.

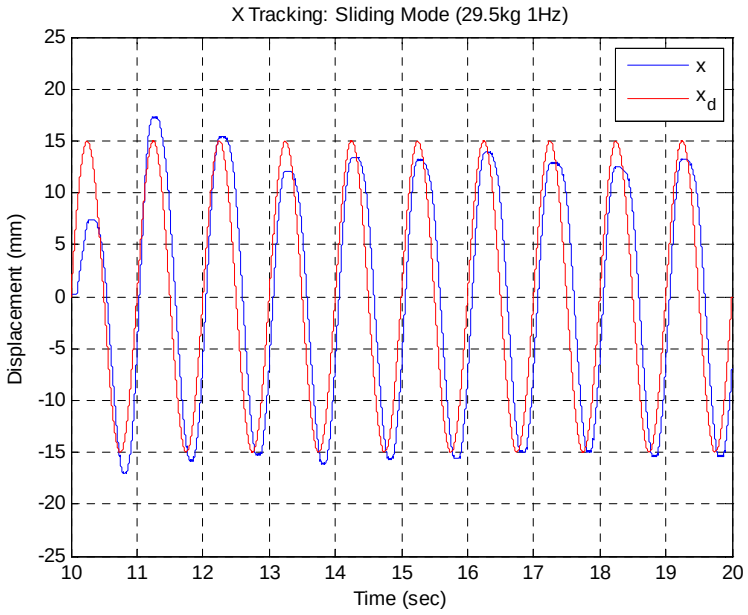

Fig. 5-1. Tracking performance of the sliding mode controller corresponding to a 1.0 Hz sinusoidal command when a 29.5kg mass is loaded.

Figure 5-2 shows experimental results of the input shaft speed, torque and power at the pump shaft when the proposed sliding mode controller is tracking a 1.0 Hz Sinusoidal command.

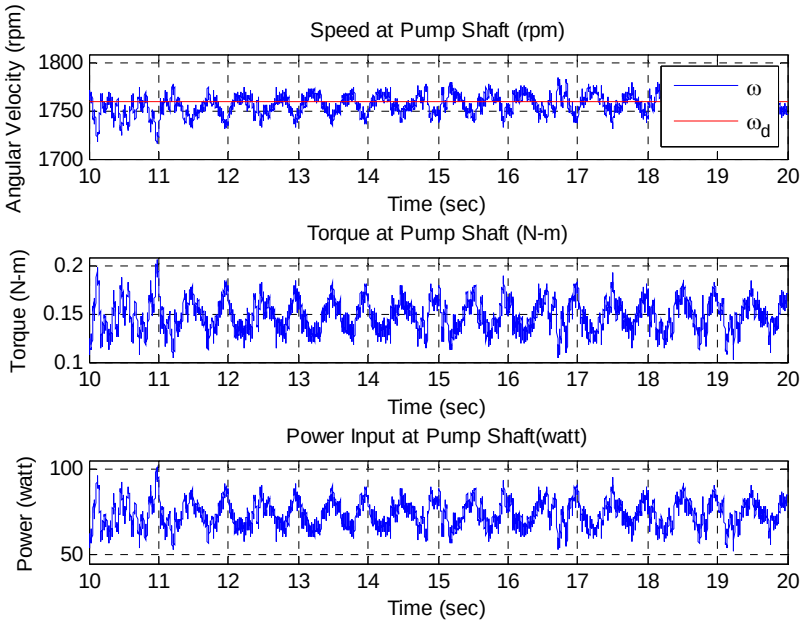

Fig. 5-2. Experimental results of the speed, torque and power input at the pump shaft when the system is tracking a 1.0 Hz Sinusoidal command.

Figure 5-3 shows the efficiencies of the system when it is tracking sinusoidal commands of different frequencies. It can be observed that the system arrives at its peak efficiency when the frequency of the desired sinusoidal position trajectory is around 1.0 Hz.

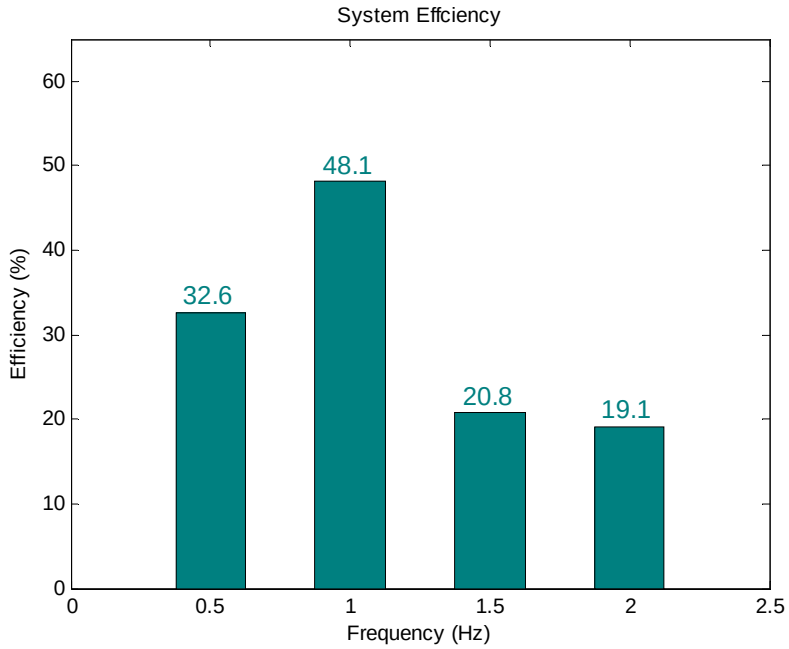

Fig. 5-3. Efficiency of system for tracking sinusoidal commands at different frequencies when sliding mode controller is implemented.

CHAPTER VI

CONCLUSION AND DISCUSSION

This thesis proposes a variable displacement pump (VDP) approach to decrease energy losses in a closed-loop controlled hydraulic actuation circuit. A vane-type VDP is proposed and described, which was specifically designed to offer a compact package for an IC engine driven multi-axis machine. The pump was fabricated and experimentally characterized, and integrated into a VDP-controlled hydraulic circuit. A PD/Smith Predictor based controller and a sliding mode controller were developed for the VDP-controlled circuit respectively, and subsequently were implemented on the experimental setup. Experimental results of the hydraulic cylinder motion tracking indicate the effectiveness of the proposed sliding mode control approach. The experiment based efficiency study shows promising potential of the proposed system in energy conservation.

REFERENCE

[1] Habibi, S., Goldenberg, A., “Design of a New High-Performance Electrohydraulic Actuator”, IEEE/ASME Transactions on Mechatronics, vol. 5, no. 2, pp. 158-64, 2000.

[2] Habibi, S., Burton, R., Sampson, E., “High Precision Hydrostatic Actuation Systems for Microand Nanomanipulation of Heavy Loads”, Transactions of the ASME, vol. 128, no. 4, pp. 778-787, 2006.

[3] Habibi, S., and Burton, R., “Parameter Identification for a High-Performance Hydrostatic Actuation System Using the Variable Structure Filter Concept”, Transactions of the ASME, Journal of Dynamic Systems, Measurement and Control, vol. 129, no. 2, pp. 229-35, 2007.

[4] Sampson, E., Habibi, S., Burton, R., Chinniah, Y., “Effect of Controller in Reducing Steady-state Error due to Flow and Force Disturbances in the Electrohydraulic Actuator System”, International Journal of Fluid Power, vol. 5, no. 2, pp. 57-66, 2004.

[5] Wang, S., Burton, R., Habibi, S., “Sliding Mode Controller and Filter Applied to a Model of an Electrohydraulic Actuator System”, American Society of Mechanical Engineers, The Fluid Power and Systems Technology Division, vol. 12 FPST, pp. 35-44, 2005.

[6] Dean, P., Fales, R., “Modern Control Design for a Variable Displacement Hydraulic Pump”, Proceedings of the 2007 American Control Conference, New York City, USA, July 2007.

[7] Perron, M., de Lafontaine, J., Desjardins, Y., “Sliding-Mode Control of a Servomotor-Pump in a Position Control Application”, CCECE/CCGEI, Saskatoon, May 2005.

[8] Grabbel, J., Ivantysynova, M., “An Investigation of Swash Plate Control Concepts for Displacement Controlled Actuators”, International Journal of Fluid Power, vol. 6, no. 2, pp. 19-36, 2005.

[9] Stefanides, E. J., “Pump/Valve System Upgrades Mobile Vehicle Hydraulics”, Design News, 2-15-82.

[10] Hydra-matic Division Service Department, “THM200-4R-Principles of Operation”, General Motors Cororation, 1980.

[11] DeGarcia, H., McDonnell Douglas Co. “Aircraft Hydraulic Systems Dynamic Analysis”, Report AFAPL-TR-78-77, Oct. 1978.

[12] Karmel, A. M., “A Study of the Internal Forces in a Variable-Displacement Vane-Pump – Part I: A Theoretical Analysis”, ASME Journal of Fluids Engineering, vol. 108, no. 2, pp. 227-232, 1986

[13] Karmel, A. M., “A Study of the Internal Forces in a Variable-Displacement Vane-Pump – Part II: A Parametric Study”, ASME Journal of Fluids Engineering, vol. 108, no. 2, pp. 233-237, 1986.

[14] Smith, O.J.M., Chem. Eng. Prog., 53, 217, 1959.

[15] Slotine, J.J.E., Li, W., “Applied Nonlinear Control”, Prentice-Hall, Inc., New Jersey, 1991.